Geophys. J. Int. (2003) **153,** 719–734

Inversion of shallow-seismic wavefields: I. Wavefield transformation

Thomas Forbriger*

Institut für Meteorologie und Geophysik, J. W. Goethe-Universität Frankfurt, Feldbergstraße 47, D-60323, *Frankfurt am Main, Germany.*
E-mail: Thomas.Forbriger@gpi.uni-karlsruhe.de

Accepted 2003 January 28. Received 2003 January 27; in original form 2002 September 10

SUMMARY

I calculate Fourier–Bessel expansion coefficients for recorded shallow-seismic wavefields using a discrete approximation to the Bessel transformation. This is the first stage of a full-wavefield inversion. The transform is a complete representation of the data, recorded waveforms can be reconstructed from the expansion coefficients obtained. In a second stage (described in a companion paper) I infer a 1-D model of the subsurface from these transforms and *P*-wave arrival times by fitting them with their synthetic counterpart. The whole procedure avoids dealing with dispersion in terms of normal modes, but exploits the full signal-content, including the dispersion of higher modes, leaky modes and their true amplitudes. It is robust even in the absence of *a priori* information. I successfully apply it to the near field of the source. And it is more efficient than direct inversion of seismograms. I have developed this new approach because the inversion of shallow-seismic Rayleigh waves suffers from the interference of multiple modes that are present in the majority of our field data sets. Since even the fundamental-mode signal cannot be isolated in the time domain, conventional phase-difference techniques are not applicable.

The potential to reconstruct the full waveform from the transform is confirmed by two field-data examples, which are recorded with 10 Hz geophones at effective intervals of about 1 m and spreads of less than 70 m length and are excited by a hammer source. Their transforms are discussed in detail, regarding aliasing and resolution. They reveal typical properties of shallow surface waves that are at variance with assumptions inherent to conventional inversion techniques: multiple modes contribute to the wavefield and overtones may dominate over the fundamental mode. The total wavefield may bear the signature of inverse or anomalous dispersion, although the excited modes have regular and normal dispersion. The resolution at long wavelengths (and thus the penetration depth of the survey) is limited by the length of the profile rather than by the signal-to-noise ratio at low frequencies.

Finally, this approach is compared with conventional techniques of dispersion analysis. This illustrates the advantage of conserving the full wavefield in contrast to the reduction to one dispersion curve.

Key words: dispersion analysis, near-field, phase-slowness, Rayleigh waves, shallow seismics, wavefield transformation.

1 INTRODUCTION

Shallow-seismic surface waves are an attractive means of investigating the mechanical properties of the subsurface in terms of shear wave velocity. Rayleigh waves are easy to excite and record with standard field equipment such as a sledge-hammer and vertical-component geophones. They have large amplitudes and thus an excellent signal-to-noise ratio. The geometry of propagation may be interpreted in two horizontal dimensions, while depth information is obtained from their frequency-dependent phase velocity. In contrast, body-wave experiments that are also able to resolve shear wave velocity are more difficult to perform in the field.

1.1 Previous studies

Early studies that specifically address shallow seismic surface waves (in the decametre range) are from the 1930s, when groups at Göttingen University and Berlin worked on civil engineering applications (Köhler 1935; Köhler & Ramspeck 1936). In the 1950s their work was carried on at Munich (Förtsch 1953; Korschunow

*Now at: Black Forest Observatory (BFO), Heubach 206, D-77709 Wolfach, Germany.

1955; Giese 1957). Bornmann (1959) published a review detailing the knowledge of that time. The processing of dispersed wave trains as well as the forward calculation of dispersion relations for stratified media was still difficult then due to the lack of electronic computing equipment. For this reason the authors did not focus on dispersion curves alone. They also discussed amplitude damping, local resonances and spatial interference of modes. And they preferred tunable harmonic vibrators as field sources.

Studies over these years remained mainly at the level of rather qualitative discussions (Howell 1949; Dobrin *et al.* 1954; Press & Dobrin 1956). However, Evison (1956) had already published a comparison between field data and synthetic waveforms.

From the 1960s onwards the academic interest of seismologists shifted to the interpretation of teleseismic surface wave data to infer upper-mantle structure. However, at that time the first papers on shallow surface wave techniques were published by Jones (1958, 1962), an author from a civil engineering background. There was a boom of geotechnical publications in the 1980s triggered by Stokoe & Nazarian (1983) and Nazarian (1984). They invented what they called the spectral analysis of surface waves (SASW) method. This technique is based on phase spectra evaluated in the field. The phase differences between two receivers are interpreted in terms of a fundamental normal-mode dispersion curve. Among these studies are many applications to the investigation of pavements. As will be demonstrated below, these must now be suspected of being disturbed by higher modes. Gucunski & Woods (1991) and Tokimatsu *et al.* (1992) first mentioned complications due to higher modes and proposed an explanation of the experimentally derived dispersion curves by an effective dispersion curve calculated under consideration of the influence of higher modes.

At the beginning of the 1990s some seismologists returned to study shallow surface waves. Gabriels *et al.* (1987) were the first to pick higher-mode dispersion curves from a wavefield spectrum. Xia *et al.* (1999) applied a conventional dispersion analysis to derive 1-D structure. Others utilized fundamental Rayleigh (Schneider & Dresen 1994; Dombrowski 1996; Misiek 1996) or Love (von Hartmann 1997) modes to infer lateral heterogeneity. Schalkwijk (1996) tried to extract shallow surface waves scattered at an underground void from seismic traces but reported complications with higher modes. Roth *et al.* (1998) observed and interpreted guided waves of large amplitude in shallow reflection data. Bohlen *et al.* (1999) and Klein *et al.* (2000) studied dispersed Scholte waves in marine shallow-seismic records.

Most of these shallow-seismic studies adopt their methodology from teleseismic studies. They calculate one phase-velocity dispersion curve from phase differences between two receivers in the data set and fit this with the fundamental normal-mode dispersion curve predicted by a hypothetical Earth model. Only a few of them recognize the importance of higher modes or even exploit their information content. There are a few more recent conference abstracts that mention the potential of shallow-seismic higher modes (Park *et al.* 1999; Beaty & Schmitt 2000; Xia *et al.* 2000). The full content of higher modes was exploited by Forbriger (2001) by an inversion of wavefield spectra. This method is presented below. Compared with teleseismic conditions, it benefits from the possibility of deploying geophones at almost any position in shallow-seismic investigations.

1.2 The concept of this study

Nine shallow-seismic field records out of 13 that I investigated show distinct higher modes. In all cases they interfere in the time domain and in some cases are even inseparable in the wavefield spectrum. In those cases, the observed dispersion cannot be interpreted in terms of dispersion relations of individual normal modes. On the other hand, an attempt to model the recorded waveforms by synthetic seismograms, which would be the direct inversion approach, fails due to the lack of *a priori* reference models for shallow-seismic sites and due to the severe non-linearity of the problem.

For these reasons I propose a two-stage inversion. In the first stage, which is described in this paper, a wavefield spectrum for the observed data set is calculated. The complex spectral amplitudes permit a reconstruction of the full waveform when used as Fourier–Bessel expansion coefficients – a procedure that may appear trivial but is not. Solving the theoretical problem of seismic wave propagation in 1-D media with common methods such as the reflectivity method (Fuchs 1968; Müller 1985) involves the calculation of synthetic Fourier–Bessel expansion coefficients. In a second stage we use such a method to fit the empirical coefficients using theoretical predictions in an iterative least-squares inversion. The latter is the subject of a companion paper (Forbriger 2003, this issue, referred to hereafter as Paper II).

As substantiated below, this two-stage spectral approach has the advantage of being less non-linear than waveform inversion and has the potential to reduce computation times by a factor of ten compared with waveform inversion. Although individual modes may be recognized in the wavefield spectrum of many data sets, their identification is not required for the inversion. Higher modes and leaky modes contribute to the result as well.

In the first part of this paper, I will review and slightly modify the slant-stack analysis as described by McMechan & Yedlin (1981) and used by Gabriels *et al.* (1987). This will be helpful in discussing aliasing and resolution properties common to all wavefield spectra. However, the slant-stack spectrum cannot be used to reproduce the waveforms in the representation of a wavefield as excited by a cylindrically symmetric point source. In the second part I will therefore describe a modified Fourier–Bessel transform that produces valid Fourier–Bessel expansion coefficients of the recorded wavefield. Finally, this approach will be compared with the results of a conventional dispersion analysis.

1.3 Example data sets

Two data sets will be used below to illustrate the data processing developed in this paper. They represent two typical classes of subsurface structure. A shot gather of the Bietigheim data set is shown in Fig. 1 and one of the Berkheim data set in Fig. 2. The traces are scaled dependent on offset to allow a comparison of amplitudes and are displayed on a reduced timescale to avoid overlap of neighbouring traces. Both data sets were recorded with 10 Hz vertical geophones. The wavefield was excited with a hammer. The data sets were combined from several single shots to enhance the receiver density. Shot gathers were scaled to compensate for differences in excitation amplitude.

The Bietigheim data set was recorded on a site with approximately 15 m of loess, loam and gravel overlying solid dolomite (Upper Muschelkalk). The subdivisions of the unconsolidated sediments are not apparent from the seismic data – no sharp discontinuities are present in the soil layer. The site was therefore regarded as a field approximation to one layer above a half-space. However, inversion exhibits a pronounced velocity gradient in the soil (Paper II).

The Berkheim data set was recorded on a hard pitch with black top pavement. The soil below the hard surface is made ground, consisting mainly of loam (Bessing, municipality Esslingen,

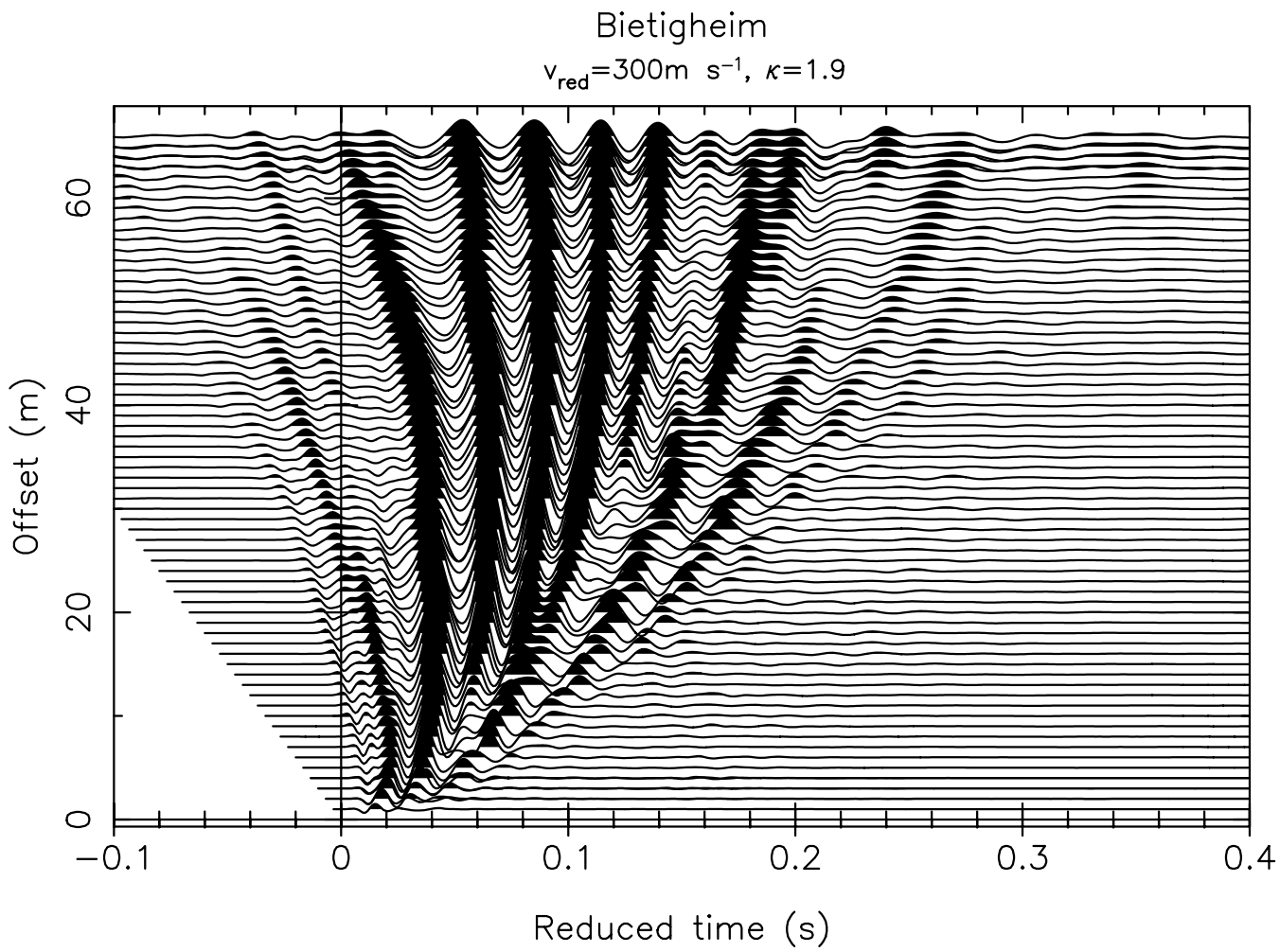

Figure 1. Bietigheim data set: raw seismogram gather. The traces are scaled with an offset-dependent factor r^{κ} and are displayed on a reduced timescale $t_{\rm red} = t - r/v_{\rm red}$. The large-amplitude signal in the centre of the wavefield constitutes the first overtone of normal modes. The fundamental mode has smaller amplitudes and makes up the tail of the dispersed wave train.

private communication, 1999). The seismic interpretation (Paper II) suggests that in about 5.5 m depth a hard layer is met. This agrees with the geological situation: in that depth a Jurassic sandstone (Lias α) may be expected. The uppermost parts of the medium show a distinct velocity inversion from the fast asphalt layer to the underlying slow soil. Consequently, the seismic waveforms show the signature of inverse dispersion: the high-frequency surface waves arrive earlier than the low-frequency ones, in contrast with the case of Fig. 1. However, as dispersion analysis shows (Fig. 10, see Section 6.2), each of the normal modes is excited in its group-slowness minimum. The characteristic of the wave train is due to the superposition of several normal modes.

2 SLANT STACK

McMechan & Yedlin (1981) describe a wavefield transformation assuming plane waves. They calculate a τ, p transform (a slant stack) of the wavefield with a subsequent Fourier transformation (p =phase slowness, τ = delay time). This yields an f, p spectrum of the wavefield (f = frequency). The surface waves become apparent in the spectrum due to their large spectral coefficients.

This method was used by several authors (Gabriels *et al.* 1987; Bohlen *et al.* 1999; Park *et al.* 1999; Klein *et al.* 2000; Beaty & Schmitt 2000; Xia *et al.* 2000) to perform the dispersion analysis of data sets that contain higher modes. I will outline this method in a slightly modified formulation and use it to explain common properties of wavefield spectra, such as aliasing and resolution.

We start from a set of N seismic waveforms $u(t, r_l)$ recorded at source–receiver offsets r_l. The slant stack of these seismograms is calculated using

$$U(\tau, p) = \sum_{l=1}^{N} u(pr_l + \tau, r_l). \tag{1}$$

Eq. (1) shifts all traces by the phase traveltime pr_l. The signal component that travels with the phase slowness p will dominate in the sum due to constructive interference. $U(\tau, p)$ can therefore be regarded as the waveform of this component.

If the seismic signal $u(t, r_l)$ is written as a Fourier integral

$$u(t, r_l) = \int_{-\infty}^{+\infty} \tilde{u}(\omega, r_l) \mathrm{e}^{-i\omega t} \frac{d\omega}{2\pi} \tag{2}$$

the slant stack, eq. (1), becomes

$$U(\tau, p) = \sum_{l=1}^{N} \int_{-\infty}^{+\infty} \tilde{u}(\omega, r_l) \mathrm{e}^{-i\omega p r_l} \mathrm{e}^{-i\omega\tau} \frac{d\omega}{2\pi}. \tag{3}$$

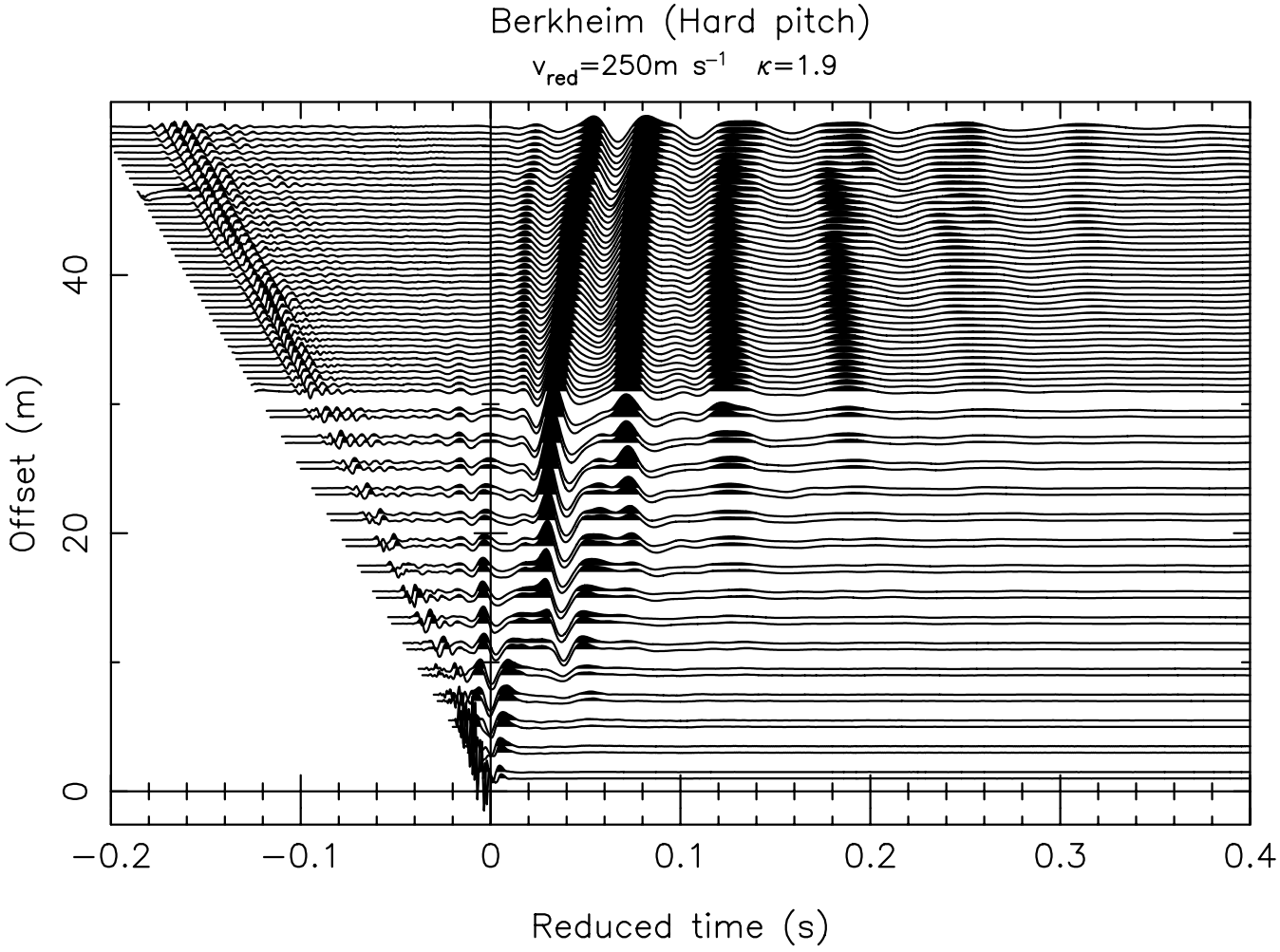

Figure 2. The Berkheim data set: raw seismogram gather. The traces are scaled with an offset-dependent factor r^{κ} and are displayed on a reduced timescale $t_{\mathrm{red}} = t - r/v_{\mathrm{red}}$. The surface waves show the signature of inverse dispersion, i.e. high frequencies arriving first at the receivers. This is due to a velocity inversion (velocity decreasing with increasing depth) in the uppermost parts of the subsurface. In this case it cannot be explained by an inversely dispersed fundamental mode. Instead it is the result of the interference of several modes.

From eq. (3) we obtain the Fourier coefficients

$$\tilde{U}(\omega, p) = \sum_{l=1}^{N} \tilde{u}(\omega, r_l) \mathrm{e}^{-i\omega p r_l} \tag{4}$$

of $U(\tau, p)$.

The amplitudes of recorded wavefields are decreasing with increasing r due to geometrical spreading, scattering and dissipative losses. Hence the contribution of terms for small r_l will dominate the stack. To gain full resolution it is best to normalize the signal energy to the offset dependence of plane waves in elastic media, which is

$$\int_0^{+\infty} u^2(t, r)\, dt = \text{constant}. \tag{5}$$

In the following I will call

$$G^{\mathrm{SLS}}(\omega, p) = \sum_{l=1}^{N} f_l \tilde{u}(\omega, r_l) \mathrm{e}^{-i\omega p r_l}, \tag{6}$$

a dispersion analysis by the slant stack, where f_l are appropriate factors to scale the seismograms to match eq. (5).

Substantial components of the seismic wavefield that travel with phase slowness p at an angular frequency ω will produce an amplitude maximum of G^{SLS} at (ω, p). The dispersion relation $p(\omega)$ of the surface waves will become apparent from these maxima. However, we may not address all of them as normal modes in the sense of elastic wave theory. Leaky modes (i.e. guided waves) and even body waves may also contribute maxima to $G^{\mathrm{SLS}}(\omega, p)$.

2.1 Noise

Seismic noise has the form of waves travelling with an unpredictable propagation direction across the geophone spread. Assuming that its sources are close to the surface, the noise signal will predominantly be surface waves. In a linear spread they will be observed with an apparent phase slowness that is smaller than their structural phase slowness $p(\omega)$ when their propagation direction is not parallel to the geophone line. The number of modes contributing to this systematic effect and thus the resulting magnitude of seismic noise increases with decreasing slowness p in $G^{\mathrm{SLS}}(\omega, p)$. Therefore, body waves with small amplitude and phase slowness are most poorly resolved, although they are present in $G^{\mathrm{SLS}}(\omega, p)$ in principle. Laterally scattered surface waves, appearing with small apparent slowness and large amplitudes in the geophone line, can often be suppressed with a time-domain taper because they appear in the coda of the direct surface waves.

2.2 Aliasing, resolution and side-lobes

As for any spectral analysis of data represented by a finite number of samples, the slant-stack dispersion analysis suffers from aliasing, limited resolution and side-lobes. This becomes obvious when analysing an impulsive plane wave

$$\tilde{u}^{\mathrm{pw}}(\omega, r_l) = \exp(i\omega p_{\mathrm{wave}} r_l) \tag{7}$$

travelling with phase slowness p_{wave} and sampled equidistantly at $r_l = l\Delta r$. Analysing eq. (7) with eq. (6) and $f_l = 1$ we obtain

$$G^{\mathrm{SLS}}(\omega, p) = \sum_{l=1}^{N} \exp[i\omega(p_{\mathrm{wave}} - p)l\Delta r]. \tag{8}$$

2.2.1 Aliasing

The amplitude of G^{SLS} for a test signal with $p_{\mathrm{wave}} = 8$ s km^{-1} is shown in Fig. 3. It has identical maxima at slowness values

$$p = p_{\mathrm{wave}} + n\frac{2\pi}{\omega\Delta r} \tag{9}$$

where n is an integer. There the terms in the sum have all the same phase (i.e. are all real and equal to unity).

The maximum with $n = 0$ is the main maximum at the wavefield slowness $p = p_{\mathrm{wave}}$. All others must be regarded as aliased because they are sampling-dependent (i.e. dependent on Δr). The smallest angular frequency at which aliasing can be found first in the interval $0 \le p \le 2p_{\mathrm{wave}}$ is

$$\omega(p_{\mathrm{wave}}) = \frac{2\pi}{\Delta r p_{\mathrm{wave}}}. \tag{10}$$

This hyperbola, which defines the aliasing limit in the (ω, p) plane, is also shown in Fig. 3. Aliasing appears first at 40 Hz where the hyperbola intersects the main maximum with $p_{\mathrm{wave}} = 8$ s km^{-1}.

2.2.2 Resolution

The amplitude of G^{SLS} is smallest (white strips in Fig. 3) at

$$p = p_{\mathrm{wave}} + n\frac{2\pi}{\omega N\Delta r}, \tag{11}$$

where the terms in the sum eq. (8) compensate each other because their phase varies from 0 to 2π when n is an integer and $n \neq 0, \pm N, \pm 2N, \ldots$.

The half-width of the main maximum can be found from eq. (11). The half distance between the neighbouring minima is

$$\Delta p = \frac{2\pi}{\omega L} \tag{12}$$

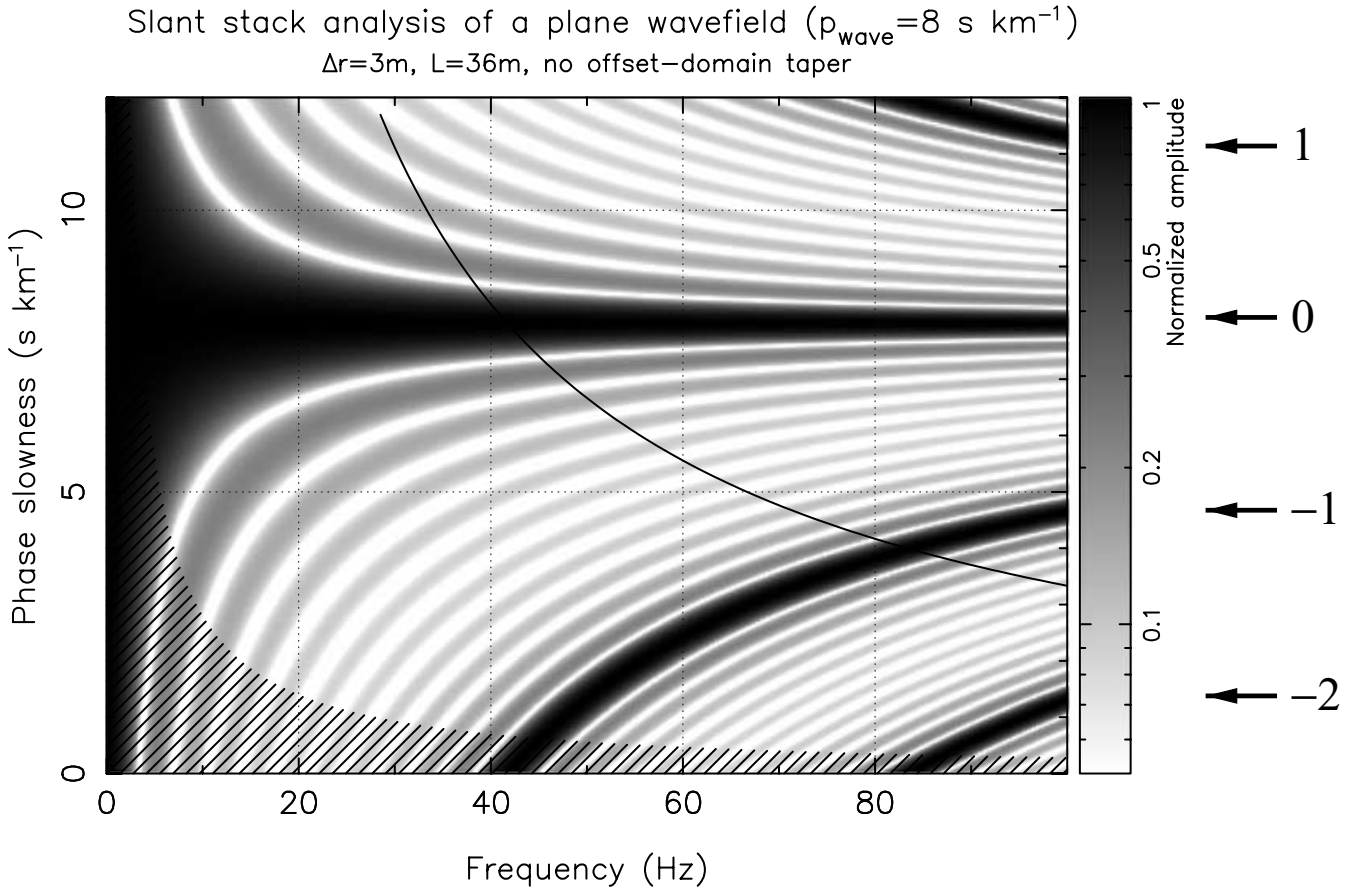

Figure 3. Slant-stack analysis of the test wavefield given in eq. (7) with $p_{\mathrm{wave}} = 8$ s km^{-1}, $\Delta r = 3$ m and $N = 12$. The maxima marked by arrows are numbered according to n in eq. (9). The main maximum at 8 s km^{-1} has $n = 0$. All others are aliased. Side-lobes, as defined by eq. (13), are visible between the pronounced maxima. Aliasing appears first at 40 Hz, where the hyperbola defined by eq. (10) intersects the main maximum with $p_{\mathrm{wave}} = 8$ s km^{-1}. The hatched area gives a measure of the theoretical width Δp of the main maximum due to a limited spread length $L = N\Delta r = 36$ m. Slowness resolution is strongly frequency dependent, becomes quickly worse at low frequencies and can only be improved by extending the geophone spread, as can be seen from eq. (12).

where $L = N\Delta r$ is the length of the geophone line. Thus eq. (12) gives a frequency-dependent limit for the resolution of the phase slowness value. It is independent of p_{wave}. Thus the relative resolution at a given frequency is worse for a smaller slowness of the wavefield.

The value of Δp is visualized by the hatched area in Fig. 3. It is strongly frequency-dependent and the resolution deteriorates rapidly at low frequencies. Since the dispersion at lower frequencies (i.e. large wavelength) bears the information concerning deeper material properties this is an effective limit to the investigation depth. It can only be influenced by the length L of the geophone spread. This, however, in practice is limited by the shallow-seismic site situation. The laterally undisturbed area in most cases is not larger than some tens to hundred metres. While the signal-to-noise ratio may still be good at frequencies between 5 and 10 Hz, the poor resolution due to a spread length of less than 100 m in most cases limits the investigation depth to about 10–20 m.

Note that eq. (12) expresses a fundamental property of phase-slowness measurements. It also applies to conventional techniques that use phase differences between Fourier coefficients at two receivers and to refraction studies. However, there it may not become apparent since normally resolution is not investigated when using these techniques. The apparent precision of such methods results only from the assumption of observing a single undisturbed mode or arrival.

2.2.3 Side-lobes

Side-lobes of the main maximum are found at

$$p = p_{\text{wave}} \pm \left(n + \frac{1}{2}\right) \frac{2\pi}{\omega N \Delta r}, \tag{13}$$

where n is a positive integer and $n \neq 0$. They may be reduced in amplitude by a smooth offset-domain taper. They are strongest in Fig. 3 because no taper was applied.

2.3 Examples

In Fig. 4 the amplitudes of the coefficients $G^{\text{SLS}}(\omega, p)$ are shown for the Bietigheim data set. We can clearly distinguish two modes of dispersive surface waves. They have an almost linear $p(\omega)$ relation above 20 Hz, which is due to a pronounced variation of seismic

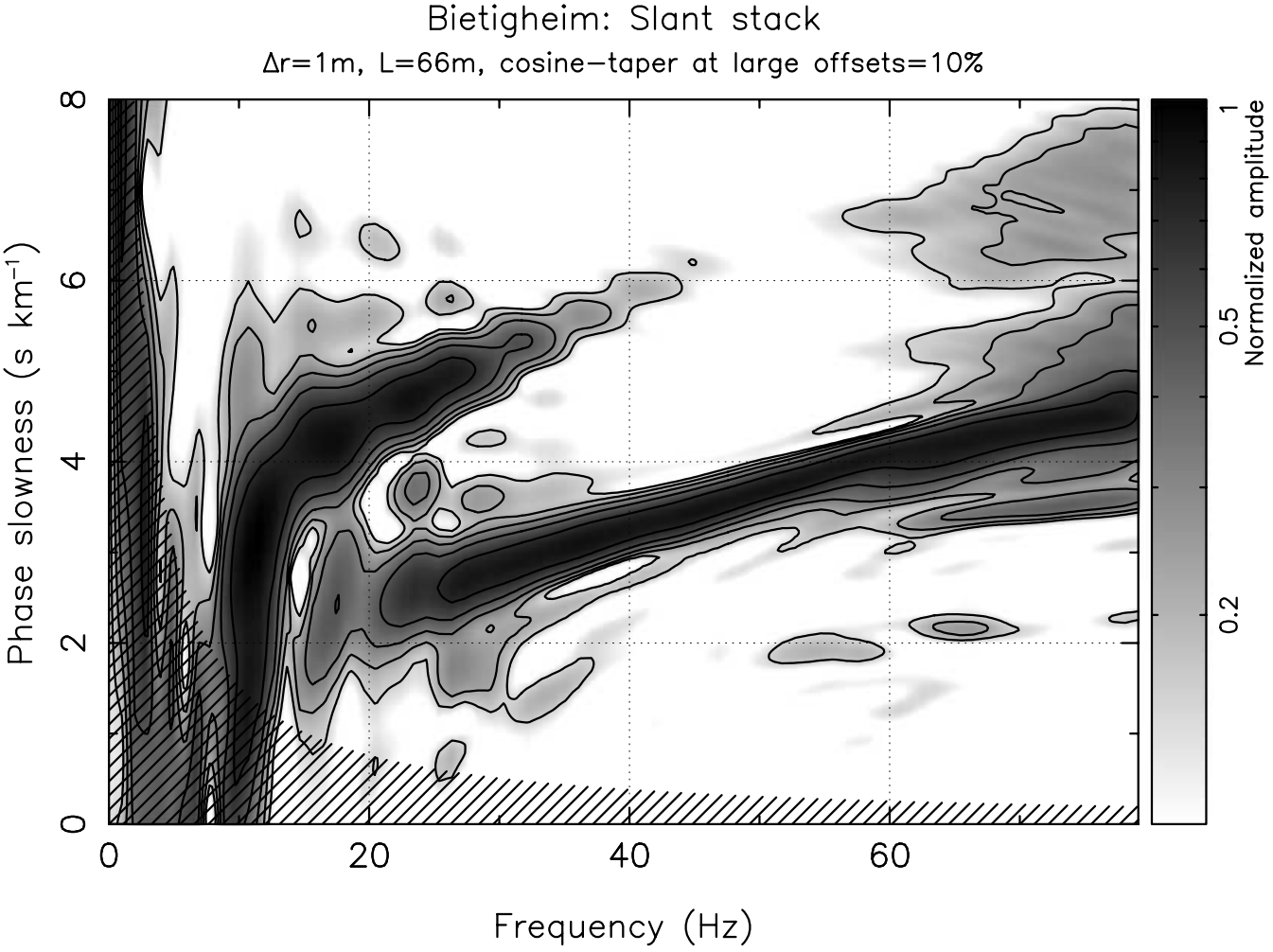

Figure 4. The Bietigheim data set: slant-stack dispersion analysis. The corresponding seismograms are shown in Fig. 1. A 10 per cent cosine taper was applied at large offsets to reduce side-lobes. The plot is scaled with a frequency-dependent factor to remove the influence of the amplitude spectrum of the source. The resolution is limited due to the geophone spread length $L = 66$ m. The minimum half-width of the maximum as a function of frequency (eq. 12) equals the width of the hatched area. Aliasing is avoided by a dense effective geophone interval of $\Delta r = 1$ m in the combined data set. Two modes are distinguishable. They have an almost linear $p(\omega)$ relationship above 20 Hz. In that frequency range the higher mode (with smaller phase slowness) clearly dominates.

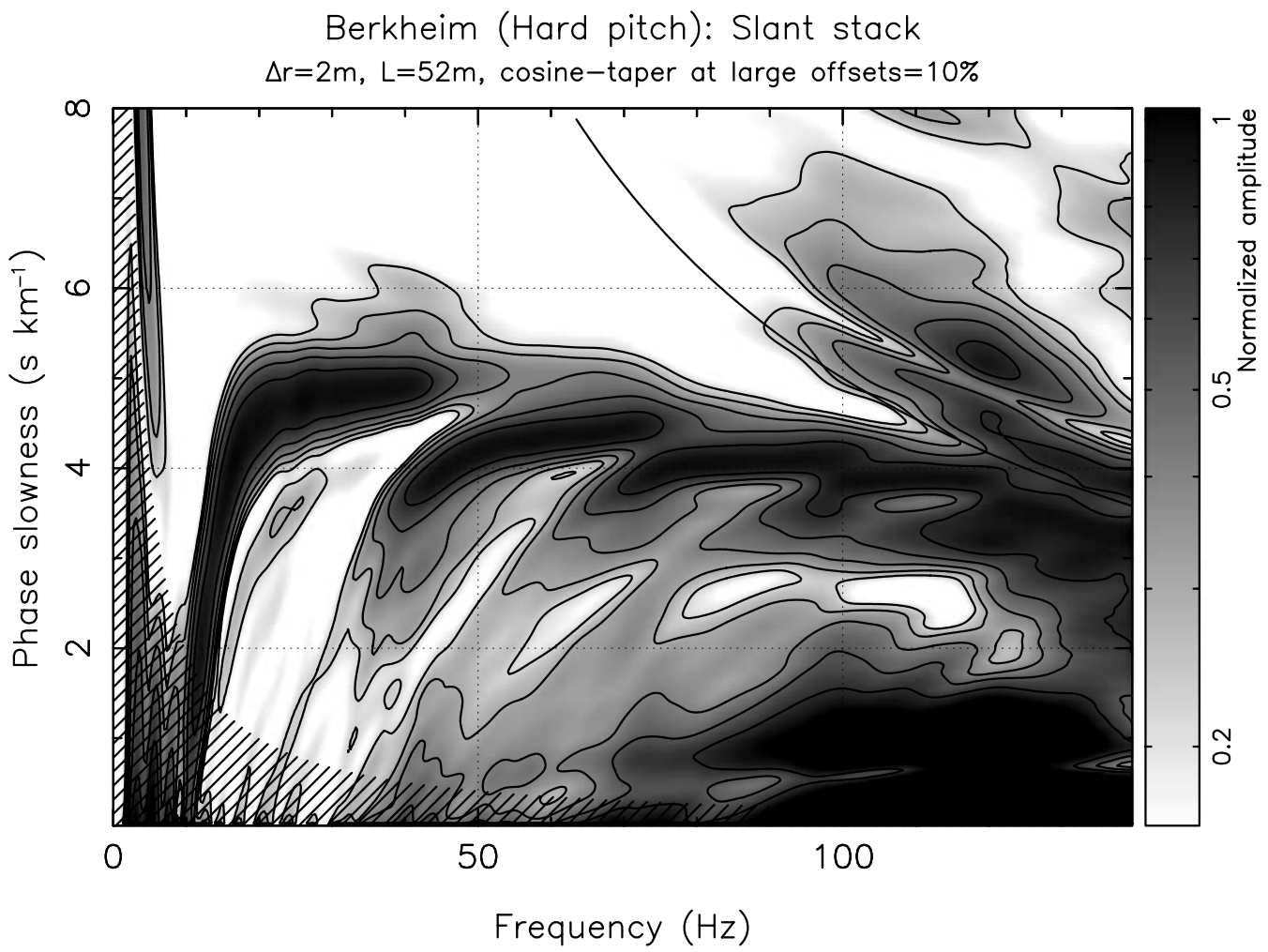

Figure 5. The Berkheim data set: slant-stack dispersion analysis. At least four modes are distinguishable that contribute to the wavefield. Each of the modes is dispersed normally (i.e. the phase slowness is increasing with increasing frequency). The combination of all modes leads to an apparently anomalous dispersion in the slant stack (i.e. the phase slowness decreases with increasing frequency). Points where dispersion curves of different modes come close to each other are called 'osculation points'. The fundamental mode and the first overtone have an osculation point at 40 Hz and 4.3 s km^{-1}. To lower frequencies the higher-mode phase slowness is decreasing rapidly, while the phase slowness of the fundamental mode increases for frequencies larger than 50 Hz. This may be established from the result of the full inversion. However, both semi-branches are not excited in the vertical component of the wavefield at the surface. The hyperbola in the plot is the aliasing limit given in eq. (10) for $\Delta r = 2$ m, which is the largest single-shot geophone interval.

velocities with depth (Paper II). The largest part of the frequency band is dominated by the higher mode with smaller phase slowness. This is in contradiction to the common assumption that the main contribution to shallow-seismic surface waves comes from the fundamental normal mode.

The amplitudes of $G^{\mathrm{SLS}}(\omega, p)$ calculated from the Berkheim data set are shown in Fig. 5. At least four modes can be clearly distinguished in the spectrum. Each mode has normal dispersion. However, the whole wavefield shows the signature of anomalous dispersion due to the combination of several normal modes.

The terms 'normal', 'anomalous', 'regular' and 'inverse' dispersion are coined to characterize the dispersion relation of one normal mode in a given frequency band. These terms may be misleading when characterizing a total wavefield, because normal modes cannot be distinguished before inversion. With a higher noise level it would be impossible to tell different modes apart in Fig. 5. The analysed data set would clearly show a character of anomalous dispersion in the slant-stack dispersion analysis and a character of inverse dispersion in the spectrogram (Fig. 10, see Section 6.2).

All figures showing wavefield spectra are scaled with a frequency-dependent factor to remove the influence of the source spectrum. Although the spectral amplitudes decrease quickly below 10 Hz, wavefields recorded with geophone spreads of more than 100 m length may show an excellent signal-to-noise ratio down to 5 Hz. In the case of Bietigheim and Berkheim the low-frequency limit is a result of the small spread length rather than the source spectrum and the receiver characteristics.

3 LIMITATION OF NORMAL-MODE INTERPRETATION

Following the conventional method of inverting shallow-seismic surface waves, we would pick a dispersion curve following the amplitude maximum of the spectrum $G^{\mathrm{SLS}}(\omega, p)$. Subsequently, we would fit this curve using the dispersion relation of the fundamental mode calculated from a hypothetical Earth model. In the same way we could also process higher modes, as was done by Gabriels *et al.* (1987).

Experience with several shallow-seismic data sets shows that problems are very likely to arise in the first step, picking the dispersion curve(s). In shallow-seismic data sets the observed dispersion cannot as easily be associated with the fundamental mode defined by elastic wave theory as in teleseismic records. The extreme material properties and contrasts in the shallow regime produce wavefields with dominating higher modes (as in the Bietigheim data set Fig. 4) and osculation points of dispersion curves (as in the Berkheim data set, Fig. 5). Also guided waves (i.e. leaky modes) may contribute with large amplitudes.

Osculation points are well known in the literature (Okal 1978; Kennett 1983, Section 11.4.1; Buchen & Ben-Hador 1996, Fig. 3b; Nolet & Dorman 1996, Fig. 3a; Dahlen & Tromp 1998, Section 11.6.2). Although their nature is seldom discussed, they are known to introduce extra complications to root-finding in the calculation of normal-mode dispersion curves (Woodhouse 1988). Sezawa & Kanai (1935) probably contributed the first discussion of an osculation point.

The modes in the Berkheim data set (Fig. 5) can only be distinguished due to excellent lateral homogeneity of the site. In similar data sets that contain more noise, the modes smear out and grow together in the spectrum at osculation points. Then it may be impossible to distinguish different modes in the slant stack. Only a full inversion of these data sets shows that several normal modes are definitely needed to explain the observed wavefield (Paper II).

In the case of Bietigheim (Fig. 4) we might misinterpret the higher (and stronger) mode as being the fundamental mode in the presence of noise or the absence of frequencies below 20 Hz (Fig. 8, see Section 6.1). The next inversion step would fit a fundamental normal mode to this higher mode. This would lead to a subsurface model with erroneous velocities and to an unrealistic Poisson's ratio in the case of joint inversion with body-wave traveltimes (Paper II).

An attractive way to overcome these complications is modelling of the full wavefield either by synthetic seismograms or by (ω, p) spectra rather than by fitting a dispersion curve. Then we need not identify normal modes in the data prior to inversion and would include higher modes and leaky modes without extra complications. Seismograms are highly non-linear and computationally intense functionals of the subsurface parameters. Initial models for shallow-seismic structures are seldom more than a first guess. Hence, in most cases a direct inversion of waveforms is not practical.

4 THE SPECTRAL APPROACH

To derive Earth model parameters from recorded shallow-seismic surface waves, I propose an inversion in the frequency and slowness domain. This requires a precise representation of the recorded wavefields in this domain. Finding it is the first stage of the inversion. The inference of subsurface parameters from the (ω, p) spectra is the second stage of the inversion, which is the subject of Paper II.

To set up an automatic inversion scheme we need to predict theoretically the wavefield excited by shallow-seismic experiments in a hypothetical medium. In this work the medium is regarded as being flat and laterally homogeneous. Furthermore, cylindrically symmetric sources (vertical hammer blow and explosion) are used. An appropriate prediction for the Fourier coefficients of the seismic waveform at offset r in this case may be written as the Bessel-function expansion

$$\tilde{u}_z(\omega, r) = \int_0^{+\infty} G_z(\omega, p) J_0(\omega p r) p \, dp \tag{14a}$$

for the vertical vector component of the wavefield and

$$\tilde{u}_r(\omega, r) = \int_0^{+\infty} G_r(\omega, p) J_1(\omega p r) p \, dp \tag{14b}$$

for the radial component. I will abbreviate eqs (14a) and (14b) by

$$\tilde{u}_\eta(\omega, r) = \int_0^{+\infty} G_\eta(\omega, p) J_\eta(\omega p r) p \, dp, \tag{15}$$

where $\eta = 0$ denotes the vertical component and $\eta = 1$ for the radial component. J_0 and J_1 are Bessel functions of the first kind and order zero and one, respectively.

The complex-valued function $G_\eta(\omega, p)$ represents the spectral coefficients of the wavefield in the frequency and slowness domain. In the case of a point source in time and space $G_\eta(\omega, p)$ may be addressed as the spectrum of the Green's function. A robust and widely used algorithm to calculate $G_\eta(\omega, p)$ is the reflectivity method (Fuchs 1968; Müller 1985).

For the second stage I propose using an inversion algorithm that fits the data in the (ω, p) domain, which has several advantages due to properties of $G_\eta(\omega, p)$.

First, the relationship between $G_\eta(\omega, p)$ and the subsurface properties (in particular, the seismic velocities) is by far less non-linear than for the waveform data. This is due to the oscillating harmonic and cylindrical functions being worked in when evaluating the expansion integrals, eqs (15) and (2). A small change in the phase slowness of a maximum in $G_\eta(\omega, p)$ may easily cause a phase shift greater than 180° in the waveform at large offsets. Thus $G_\eta(\omega, p)$ is much easier to linearize for an iterative least-squares scheme than the waveform. And there is less risk of being trapped by local minima of the objective function.

Secondly, the theorems of discrete spectral analysis tell us that a set of seismograms at N different offsets r_l does not contain more information than for resolving $G_\eta(\omega, p_j)$ at N different wavenumbers $k_j = \omega p_j$. In a typical survey N is about 24–100. However, to calculate waveforms by numerical integration of eq. (15) we would typically need 500–2000 coefficients $G_\eta(\omega, p_j)$ per frequency to obtain accurate results. Since fitting the data in the (ω, p) domain avoids the evaluation of eq. (15) it has the potential to decrease the computation times by a factor of ten. If partial derivatives are approximated by finite differences, an extra calculation of all $G_\eta(\omega, p)$ for each single model parameter is necessary. The overall computation time then almost only depends on the numerical effort spent on the calculation of the $G_\eta(\omega, p)$ coefficients.

Thirdly, to work in the (ω, p) domain facilitates the construction of an initial model, which still must be done by trial and error. While multiple modes interfere in the oscillating time series, they can often be separated in the (ω, p) domain.

In order to carry out the fit in the (ω, p) domain we first need a method to calculate spectral coefficients $G_\eta(\omega, p)$ that reproduce the recorded data in eq. (15). Additionally, $G_\eta(\omega, p)$ should interpolate the wavefield between the r_l by a wave propagating away from the source. Below I will discuss a modification of the Bessel transformation that meets these requirements. The slant stack $G^{\mathrm{SLS}}(\omega, p)$ cannot be used to reproduce the wavefield excited by a point source in the expansion (15).

5 MODIFIED FOURIER–BESSEL TRANSFORM

Eq. (15) may be addressed as one part of the symmetric Bessel transformation (Sommerfeld 1978, Section 21.8a) that is derived from the Fourier–Bessel integral

$$f(r) = \int_0^{+\infty} J_n(kr) \int_0^{+\infty} f(r') J_n(kr') r'\, dr'\, k\, dk, \tag{16}$$

where n is any integer order (Ben-Menahem & Singh 1981; Morse & Feshbach 1953, eqs D.29 and 6.3.62, respectively). The inverse to eq. (15) are simply the (ω, p) coefficients

$$G_\eta(\omega, p) = \omega^2 \int_0^{+\infty} \tilde{u}_\eta(\omega, r) J_\eta(\omega p r) r\, dr \tag{17}$$

derived from the Fourier coefficients of the seismograms in straightforward calculation. In practice we do not know the continuous wavefield $\tilde{u}_\eta(\omega, r)$. Since there exists no corresponding discrete form for the Bessel transformation, we approximate eq. (17) by

$$G_\eta(\omega, p) = \omega^2 \sum_{l=1}^{N} \tilde{u}_\eta(\omega, r_l) J_\eta(\omega p r_l) r_l \Delta r_l, \tag{18a}$$

where

$$\Delta r_l = \frac{1}{2} \begin{cases} r_2 - r_1 & \text{for } l = 1, \\ r_N - r_{N-1} & \text{for } l = N \text{ and} \\ r_{l+1} - r_{l-1} & \text{otherwise} \end{cases} \tag{18b}$$

with $r_{l+1} \geq r_l$ corresponds to the trapezoid rule.

The r_l are predefined by the field configuration. We may not expect them to ensure an accurate approximation of eq. (17) by eq. (18) for all frequencies. However, as experience shows, the approximation is acceptable for practical usage if we replace the Bessel-function $J_\eta = (H_\eta^{(1)} + H_\eta^{(2)})/2$ by the Hankel-function $H_\eta^{(2)}/2$ alone and thus modify eq. (18a) to give

$$G_\eta^{\mathrm{BTR}}(\omega, p) = \frac{\omega^2}{2} \sum_{l=1}^{N} \tilde{u}_\eta(\omega, r_l) H_\eta^{(2)}(\omega p r_l) r_l \Delta r_l. \tag{19}$$

5.1 Outgoing and incoming waves

The motivation to omit the Hankel-function $H_\eta^{(1)}$ in eq. (19) follows from a closer look at the aliasing arising from eq. (18). Eq. (18a) may be rewritten as

$$G_\eta(\omega, p) = \frac{\omega^2}{2} \sum_{l=1}^{N} \left[H_\eta^{(1)}(\omega p r_l) + H_\eta^{(2)}(\omega p r_l) \right] \times \tilde{u}_\eta(\omega, r_l) r_l \Delta r_l \tag{20}$$

using the Hankel functions $H_\eta^{(1)}$ and $H_\eta^{(2)}$. Moreover, we express the Hankel functions by

$$H_\eta^{(1)}(x) = M_\eta(x) \exp[i \Theta_\eta(x)] \tag{21a}$$

and

$$H_\eta^{(2)}(x) = M_\eta(x) \exp[-i \Theta_\eta(x)], \tag{21b}$$

respectively, where the modulus $M_\eta(x)$ and the phase $\Theta_\eta(x)$ are real functions (Abramowitz & Stegun 1972, eq. 9.2.17). Now we analyse an outward propagating cylindrical wavefield

$$\tilde{u}_\eta(\omega, r_l) = H_\eta^{(1)}(\omega p_{\mathrm{wave}} r_l), \tag{22}$$

which leads to

$$G_\eta(\omega, p) = \frac{\omega^2}{2} \sum_{l=1}^{N} \Bigg\{ \underbrace{\exp[i \Theta_\eta(\omega p_{\mathrm{wave}} r_l) + i \Theta_\eta(\omega p r_l)]}_{①} + \underbrace{\exp[i \Theta_\eta(\omega p_{\mathrm{wave}} r_l) - i \Theta_\eta(\omega p r_l)]}_{②} \Bigg\} \times \underbrace{M_\eta(\omega p_{\mathrm{wave}} r_l) M_\eta(\omega p r_l) r_l}_{③} \Delta r_l. \tag{23}$$

The term ① is due to $H_\eta^{(1)}$ and ② is due to $H_\eta^{(2)}$ in eq. (20). Since a first-order approximation gives $M_\eta^2(x) \approx 2/(\pi x)$, the factor ③ will give a contribution of the same magnitude at every l. The result of the summation in eq. (23) is mainly determined by terms ① and ②. The phase $\Theta_\eta(x)$ is an antisymmetric, increasing monotonic function (Abramowitz & Stegun 1972 , eq. 9.2.21). Thus, as discussed above for eq. (8), in most cases the values of the exponential functions will be distributed over the complex unit circle and compensate each other in the sum. However, for $p = -p_{\mathrm{wave}}$ or p_{wave} term ① or ②, respectively, is independent of l and gives a major contribution to the sum.

Furthermore, we replace the phase by its far-field approximation $\Theta_\eta(x) \approx x - (\eta/2 + 1/4)$ and choose $r_l = l\ \Delta r$. Then,

$$① \approx \exp[i \omega l \Delta r (p_{\mathrm{wave}} + p)] \exp[-i(2\eta + 1)/2] \tag{24}$$

and

$$② \approx \exp[i \omega l \Delta r (p_{\mathrm{wave}} - p)]. \tag{25}$$

Analogous to the discussion of eq. (8) we find major contributions to the amplitude of $G_\eta(\omega, p)$ in eq. (23) for

$$p = -p_{\mathrm{wave}} + n \frac{2\pi}{\omega \Delta r} \tag{26}$$

due to ① and for

$$p = p_{\mathrm{wave}} + n \frac{2\pi}{\omega \Delta r} \tag{27}$$

due to ② for all integer n. Again the amplitude maxima for $n = 0$ are the main peaks, whereas maxima with $n \neq 0$ are Δr-dependent and must be addressed as aliasing. The latter vanish as we approach the continuous case (i.e. $\Delta r \to 0$).

For $G^{\mathrm{SLS}}(\omega, p)$ in eq. (8) we only found the condition (27) (which is identical to eq. 9). In the construction of eq. (8) we only considered waves travelling away from the source. However, in the general case (as represented by eq. 18 or 20) a finite set of seismograms may be understood as outgoing waves as well as waves cumulating at the source. This is the origin of term ①, which adds a significant disturbance to $G_\eta(\omega, p)$ with its aliasing for $n > 0$ at positive slowness p.

We get rid of this by using eq. (19) rather than eq. (18a). An exact mathematical treatment has not been found because it involves integrals of products of cylindrical functions of different type, which cannot be solved analytically. However, the discussed properties become plausible through the example in Fig. 6.

5.2 Examples and wavefield reconstruction

The ambiguity inherent in eq. (18) is illustrated in Fig. 6. The three panels on the left show different versions of the Bessel transform analysis of a single shot from the Bietigheim data set. The top

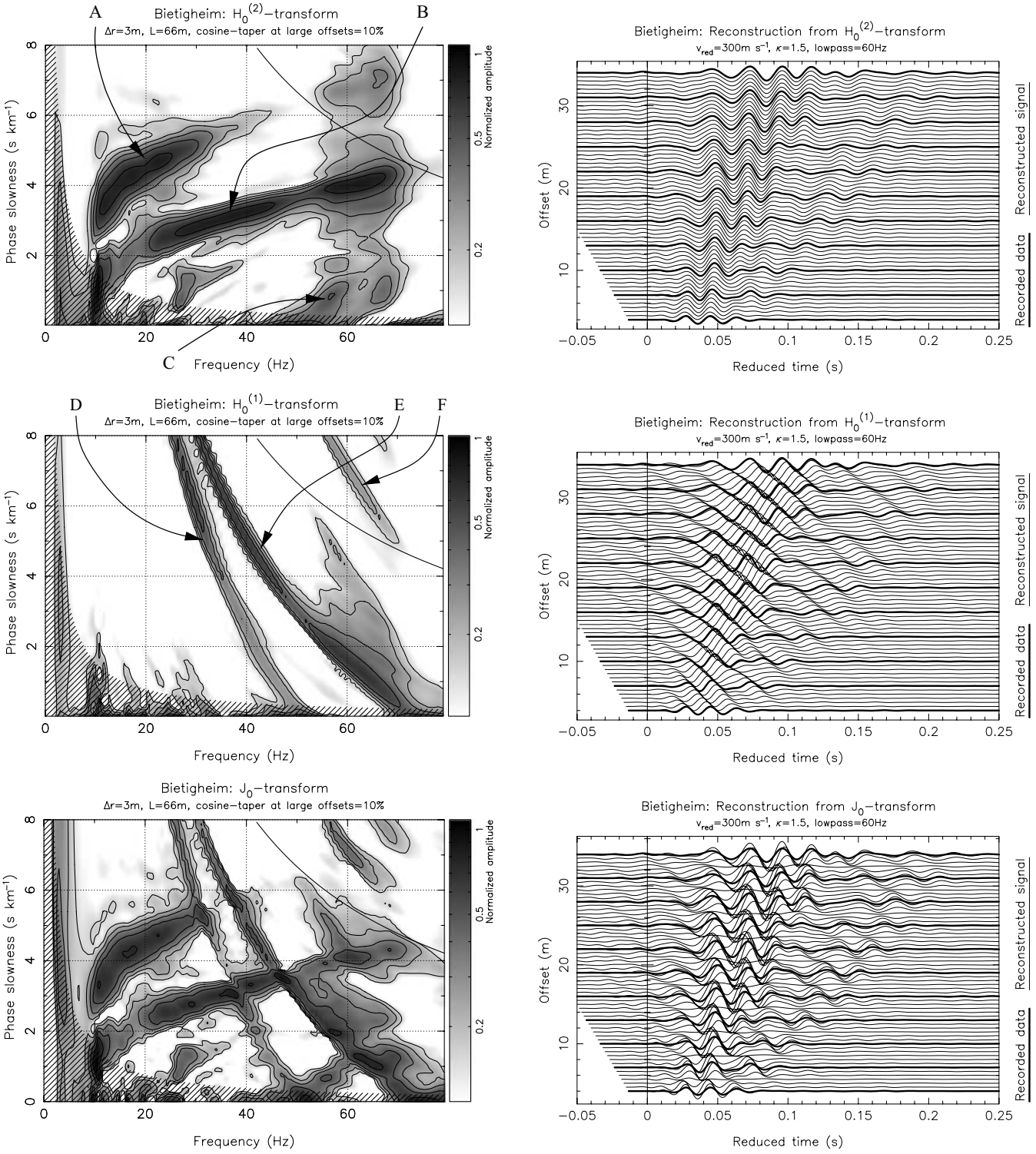

Figure 6. The Bietigheim data set: analysis and reconstruction of single-shot seismograms. The grey-scale gives the amplitudes of the $G_z^{\mathrm{BTR}}(\omega, p)$ spectrum calculated using eq. (19) from the seismograms. Recorded seismograms (thick lines) are superimposed on the reconstructed waveforms in the right-hand panels. Top left: the Bietigheim data set analysed by eq. (19). A, fundamental mode main peak ($n = 0$ in eq. 27); B, higher-mode main peak ($n = 0$ in eq. 27); C, fundamental mode alias peak with $n = -1$ in eq. (27). Top right: waveforms reconstructed by inserting the $G_z^{\mathrm{BTR}}(\omega, p)$ spectrum (top left) into the expansion (14a). The reconstructed waveforms interpolate the recorded data using outgoing waves. At the geophone offsets of the field experiment they cannot be distinguished from the superimposed data. Middle left: the Bietigheim data set analysed using eq. (19) and with $H_0^{(2)}$ replaced by $H_0^{(1)}$. D, the fundamental mode alias peak with $n = 1$ in eq. (26); E, the higher-mode alias peak with $n = 1$ in eq. (26); F, the higher-mode alias peak with $n = 2$ in eq. (26). Middle right: the reconstructed wavefield is interpolated using waves with a negative phase velocity of unphysical meaning. The waves still propagate with a positive group velocity. Bottom left: the Bietigheim data set analysed using eq. (18a). This is equal to a superposition of the above panels. Bottom right: the reconstructed wavefield is severely disturbed by waves with a negative phase velocity. It is interpolated using non-propagating waves.

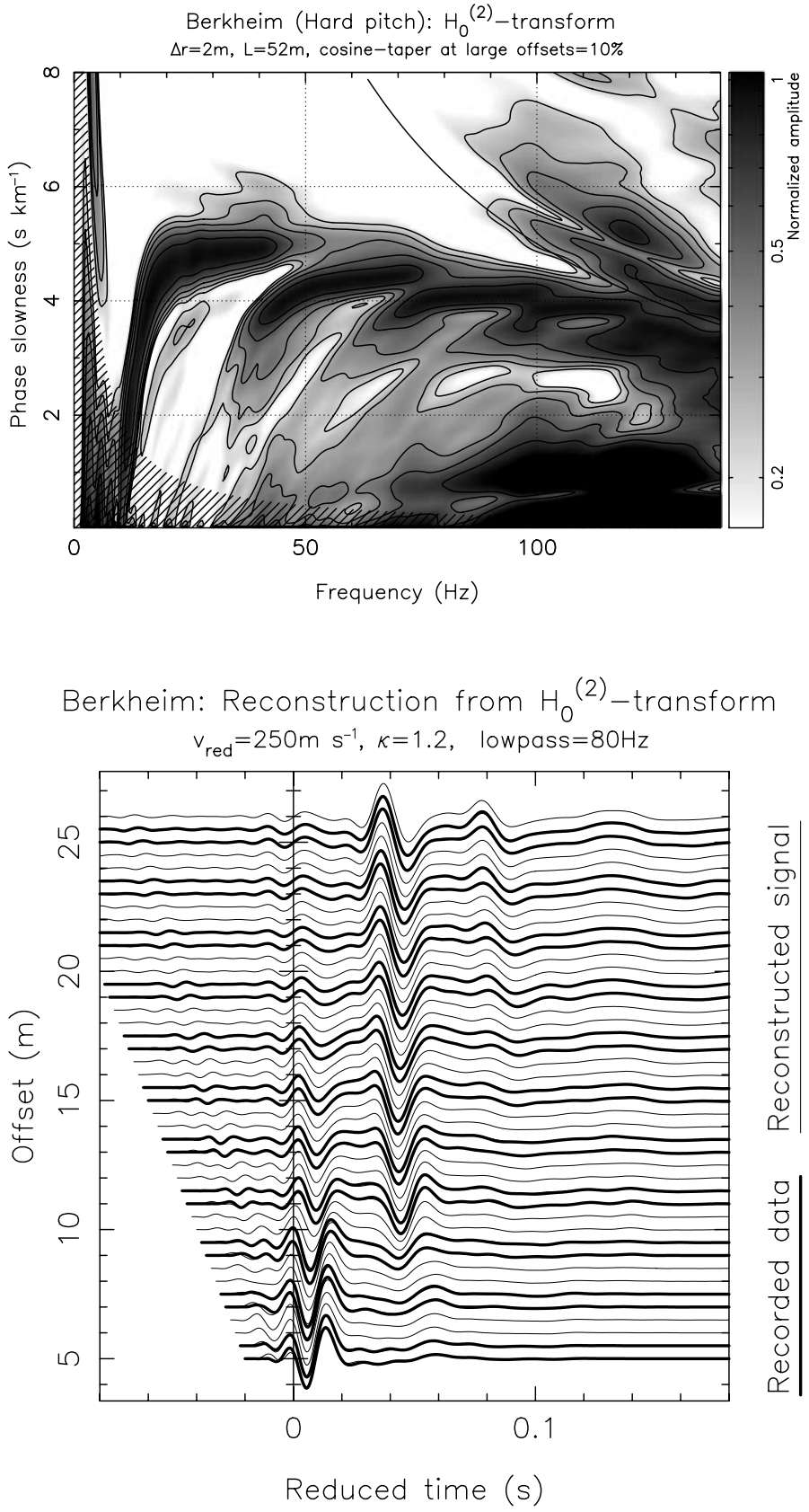

Figure 7. The Berkheim data set: a Bessel-transform analysis and reconstruction of waveforms. Top: the grey-scale gives the amplitude of the $G_z^{\mathrm{BTR}}(\omega, p)$ spectrum calculated using eq. (19) from the seismograms shown in Fig. 2. See Fig. 5 for a discussion of modes. Bottom: the seismograms were calculated by inserting the $G_z^{\mathrm{BTR}}(\omega, p)$ spectrum displayed in the top figure into the expansion (14a). Recorded waveforms (thick lines) are superimposed. Only in the body waves at small offsets can they be distinguished from the reconstructed signal.

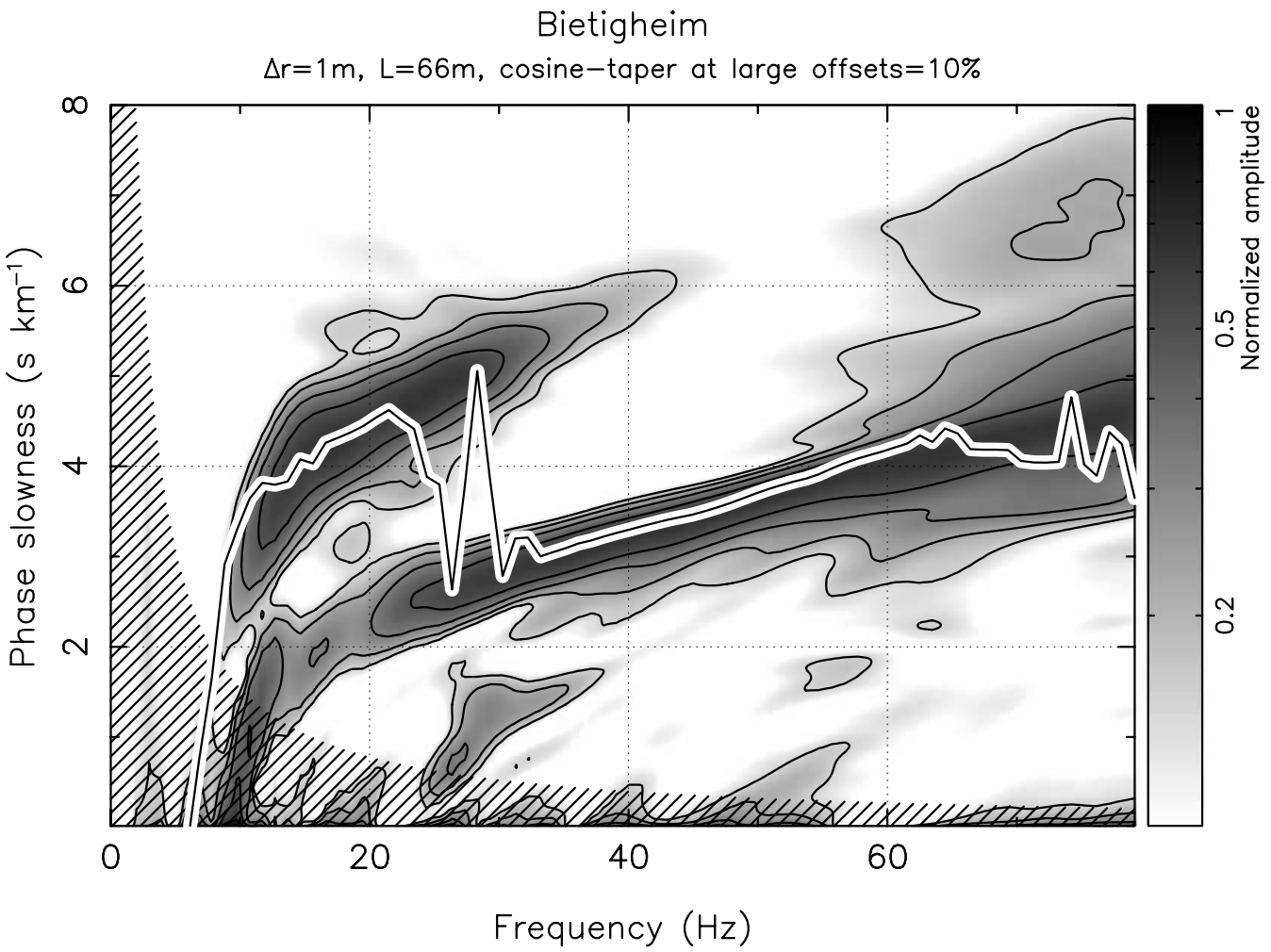

Figure 8. The Bietigheim data set: G_z^{BTR} spectrum and conventional dispersion analysis. The grey-scale image shows the amplitudes of a wavefield spectrum calculated using eq. (19) from the Bietigheim data set. The superimposed dispersion curve was calculated using the phase-slowness analysis technique described in the appendix. Interference of two modes of similar amplitude leads to jumps of the dispersion curve around 30 Hz. The seismograms were tapered before the analysis to remove body-wave onsets and surface wave coda. For frequencies larger than 50 Hz the phase increment in eq. (A3) was forced to be positive.

spectrum is $G_z^{\mathrm{BTR}}(\omega, p)$, calculated using eq. (19). As already discussed for Fig. 4 we can identify a fundamental mode and a higher mode. The spectrum in the middle was calculated using eq. (19), but with $H_0^{(2)}$ replaced by $H_0^{(1)}$. Three maxima are marked, which are aliasing according to term ① in eq. (23) with $n = 1$ (D and E in Fig. 6) and $n = 2$ (F) in eq. (26), respectively. The bottom panel shows the result of the discretized Bessel transformation as defined by eq. (18). This is essentially a superposition of the two spectra above.

The panels on the right show the waveforms calculated from the spectra on the left by inserting them in the expansion integrals (14a) and (2). The Bessel expansion eq. (14a) can be evaluated numerically to arbitrary precision since $G_z^{\mathrm{BTR}}(\omega, p)$ can be calculated at any p. The recorded seismograms are superimposed. The $G_z^{\mathrm{BTR}}(\omega, p)$ spectrum at the top reconstructs and interpolates the recorded waveforms very well. They are indeed indistinguishable from the superimposed data. The $H_0^{(1)}$ version in the middle panel, in contrast, interpolates with waves of negative phase velocity of unphysical meaning. The group velocity is still positive, which is essential to reconstruct the recorded waveforms at r_1. As can be seen in the bottom panel, the discretized version of the Bessel transformation, i.e. eq. (18), does not produce a successful representation of the wavefield. It is significantly disturbed by the aliasing of term ① in eq. (23), which is represented by the middle panels. It is even unable to reconstruct the waveforms at the original offsets reasonably. Hence, we prefer the modified Bessel transform, eq. (19), which results in $G_z^{\mathrm{BTR}}(\omega, p)$ as shown in the top panels.

Fig. 7 shows the amplitudes of $G_z^{\mathrm{BTR}}(\omega, p)$ calculated using eq. (19) from the Berkheim data set (Fig. 2). As discussed for Fig. 5, several modes may be distinguished that contribute to the wavefield. The complex coefficients have the potential to reconstruct the recorded waveforms when inserted in the expansion integrals (14a) and (2). This is confirmed by the waveforms in Fig. 7, where recorded seismograms are superimposed on the reconstructed signals. Only for the body waves at small offsets do both signals depart slightly from each other.

6 COMPARISON WITH CONVENTIONAL TECHNIQUES

To emphasize the potential of the proposed method, I will finally compare it with conventional techniques widely used for dispersion analysis (Dziewonski & Hales 1972; Kovach 1978).

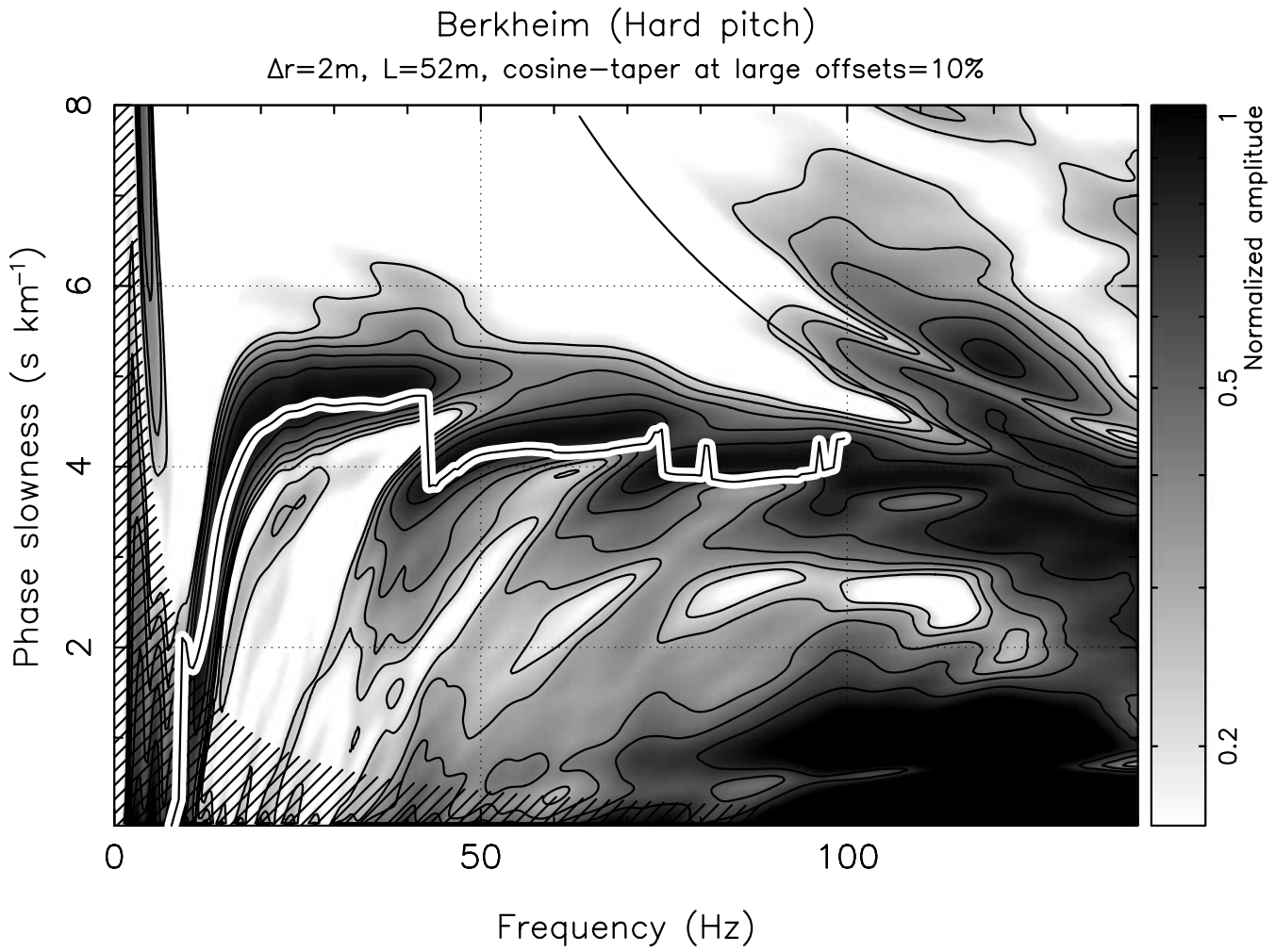

Figure 9. The Berkheim data set: G_z^{BTR} spectrum and conventional dispersion analysis. The grey-scale image shows the amplitudes of a wavefield spectrum calculated with eq. (19) from the Berkheim data set. The superimposed dispersion curve was calculated using the phase-slowness analysis technique described in the appendix. Since the contribution of several modes to the wavefield varies with frequency, the phase-slowness dispersion curve jumps. The seismograms were tapered before the analysis to remove body-wave onsets and surface wave coda. For frequencies greater than 60 Hz the phase increment in eq. (A3) was forced to be positive.

6.1 Phase-slowness analysis

If a single-mode plane wave can be extracted from the waveforms, its phase-velocity dispersion can be derived from phase differences between Fourier coefficients at different offsets (see the Appendix). However, in the case of multimode data sets the result of such techniques may become ambiguous or even misleading. Fig. 8 shows the $G_z^{\mathrm{BTR}}(\omega, p)$ spectrum of the Bietigheim data set with a conventionally derived dispersion curve superimposed. A similar plot for the Berkheim data set is shown in Fig. 9.

The sudden jumps of the dispersion curves to smaller phase slowness values indicate the influence of higher modes. However, in the absence of a sufficient signal-to-noise ratio in the data below 25 Hz, we would probably interpret the higher mode of the Bietigheim data set as a fundamental mode. Only a subsurface model with unrealistic material properties (a negative Poisson ratio) could describe the dispersion as a fundamental mode and the *P*-wave onsets at the same time (Paper II).

Applying the phase-difference method to a data set such as Berkheim, but with worse noise conditions, would apparently indicate a decreasing phase-slowness dispersion curve of a single mode. However, it is impossible to find a 1-D subsurface model that explains the wavefield of the Berkheim data set with single-mode dispersion (Paper II).

Note that the situation becomes even worse when using phase differences between only two receivers (as is usual with SASW). Since deriving the phase of the signal involves the application of a non-unique inverse of the complex exponential function, phase jumps will then be interpreted as increasing phase slowness rather than as a sudden jump to a different mode with smaller phase slowness. For a receiver distance of 25 m the jump of about 1 s km^{-1} at 40 Hz (Fig. 9) would be completely invisible.

6.2 Group-slowness analysis

A conventional technique appropriate for multimode data sets is the interpretation of group-arrival times. They can be read from a spectrogram (sometimes called a 'Gabor matrix') as shown in Fig. 10 for the Berkheim data set (the calculation is outlined in the appendix). The amplitude maxima define the arrival of wavegroups of the given frequency at an offset of 51.5 m. Dividing the arrival

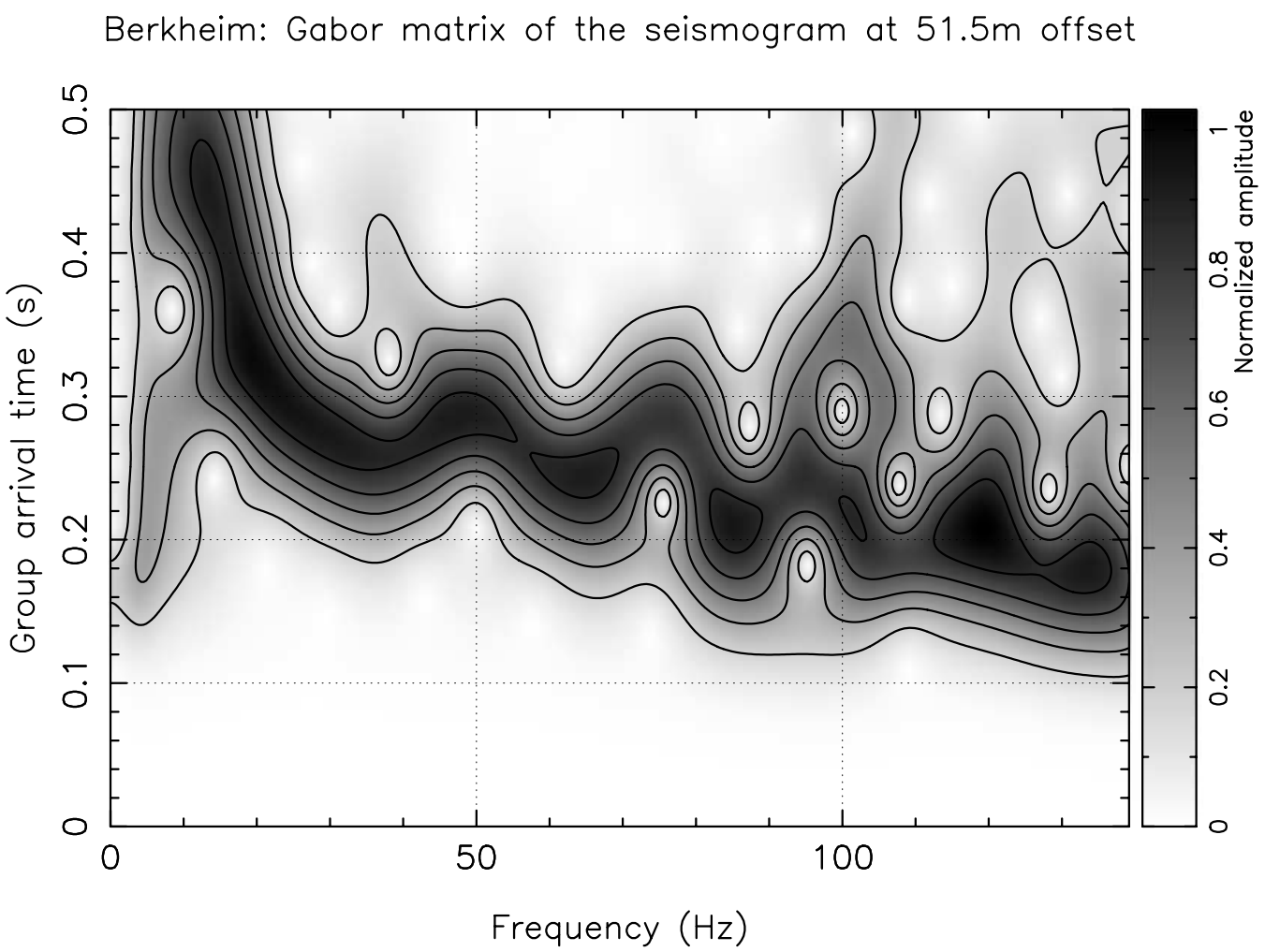

Figure 10. The Berkheim data set: spectrogram (Gabor matrix) of trace no 72 at 51.5 m offset. Amplitudes as given by the grey values are scaled as frequency-dependent to remove the influence of the source spectrum. Scaling the time axis with the reciprocal offset immediately leads to a group-slowness dispersion plot. As a result of the crossing of dispersion curves, the multimode character of the data set does not become obvious. However, by a comparison with the G^{BTR} spectrum in Fig. 9 it becomes recognizable that each mode is excited in its group-slowness minimum. The Gabor matrix alone shows an apparently inverse dispersion (i.e. the group slowness decreases with increasing frequency) as discussed for the waveforms in Fig. 2. The waveform was tapered before the analysis to remove body-wave onsets and the surface wave coda.

time by the offset immediately leads to a group-slowness dispersion curve. However, the multimode character of the data set does not become apparent from Fig. 10 (in contrast to the phase-slowness spectra in Figs 5, 7 and 9) because group-slowness dispersion curves may cross each other arbitrarily. Again we could tend to interpret the wavefield dispersion as a single inversely dispersed fundamental mode.

7 CONCLUSIONS AND OUTLOOK

The two example data sets, Bietigheim and Berkheim, have properties that are typical for most of our shallow-seismic field-data sets: multiple Rayleigh modes interfere in the wavefield. Even the fundamental mode cannot be separated in the time domain and higher modes dominate in some frequency ranges. Thus, conventional phase-difference techniques to determine a dispersion relation are not applicable.

Furthermore, it may be impossible to identify normal modes in the spectrum of the observed wavefield, due to osculation points, noise and a lack of mode excitation. Leaky modes are not distinguishable from normal modes in the wavefield spectrum. Therefore, I propose a two-stage inversion that fits the observed wavefield by synthetic predictions in terms of Fourier–Bessel expansion coefficients. This method exploits the full signal content, including the dispersion of higher modes, leaky modes and their true amplitudes. It is by far less non-linear and more efficient than waveform fitting.

In this paper I developed a modified Bessel transformation that allows the calculation of Fourier–Bessel expansion coefficients from a discrete set of seismograms excited by a point source. Examples have confirmed that the coefficients determined from eq. (19) are capable of reconstructing the full recorded wavefield in the waveform domain. They are an equivalent representation of the recorded data and thus may be fitted by synthetic predictions. This second stage of wavefield inversion is described in a companion paper (Forbriger 2003, this issue).

ACKNOWLEDGMENTS

I thank Erhard Wielandt and Wolfgang Friederich for their continued interest in this work, their thorough reviews of the manuscript

and constructive comments. I am especially grateful to Gerhard Müller. Until his early death he expressed much interest in my work and gave valuable advice on an early version of the manuscript. Furthermore, I gratefully acknowledge the contribution of Stefan Hecht and Gunther Reimann to the field work and comments on the manuscript by Ingi Bjarnason. I thank Wolfgang Rabbel and an anonymous reviewer for their encouraging comments. This study was supported by the Institute of Geophysics at the University of Stuttgart.

REFERENCES

Abramowitz, M. & Stegun, I.A., eds, 1972. *Handbook of Mathematical Functions,* 9th edn, Dover, New York.

Beaty, K.S. & Schmitt, D.R., 2000. A study of near-surface seasonal variability using Rayleigh wave dispersion, in *70th Ann. Int. Mtg, Expanded Abstracts,* pp. 1323–1326, Society of Exploration Geophysicists.

Ben-Menahem, A. & Singh, S.J., 1981. *Seismic Waves and Sources,* Springer, New York.

Bohlen, T., Klein, G., Duveneck, E., Milkereit, B. & Franke, D., 1999. Analysis of dispersive seismic surface waves in submarine permafrost, in *61st Conf. and Technical Exhibitions, Expanded Abstracts,* EAGE.

Bornmann, G., 1959. Grundlagen und Auswerteverfahren der dynamischen Baugrundseismik, *Diplomarbeit,* Bergakademie Freiberg (Sachsen), Germany.

Buchen, P. & Ben-Hador, R., 1996. Free-mode surface-wave computations, *Geophys. J. Int.,* **124,** 869–887.

Dahlen, F.A. & Tromp, J., 1998. *Theoretical Global Seismology,* Princeton University Press, Princeton, NJ.

Dobrin, M.B., Lawrence, P.L. & Sengbush, R.L., 1954. Surface and near-surface waves in the Delaware basin, *Geophysics,* **19,** 695–715.

Dombrowski, B., 1996. 3D-modeling, analysis and tomography of surface wave data for engineering and environmental purposes, *Dissertation,* Institut für Geophysik, Ruhr-Universität Bochum.

Dziewonski, A.M. & Hales, A.L., 1972. Numerical analysis of dispersed seismic waves, in *Methods in Computational Physics, Seismology: Surface Waves and Earth Oscillations,* Vol. 11, pp. 39–85, ed. Bolt, B.A., Academic, New York.

Evison, F.F., 1956. Seismic waves from a transducer at the surface of stratified ground, *Geophysics,* **21,** 939–959.

Forbriger, T., 2001. Inversion flachseismischer Wellenfeldspektren, *Dissertation,* Institut für Geophysik, Universität Stuttgart, URL: http://elib.uni-stuttgart.de/opus/volltexte/2001/861.

Forbriger, T., 2003. Inversion of shallow-seismic wavefields: II. Inferring subsurface properties from wavefield transforms, *Geophys. J. Int.,* **153,** 736–753 (this issue).

Förtsch, O., 1953. Deutung von Dispersions- und Absorptionsbeobachtungen an Oberflächenwellen, *Gerl. Beitr. z. Geophys.,* **63,** 16–58.

Fuchs, K., 1968. The reflection of spherical waves from transition zones with arbitrary depth-dependent elastic moduli and density, *J. Phys. Earth,* **16,** 27–41(special issue).

Gabriels, P., Snieder, R. & Nolet, G., 1987. *In situ* measurements of shear-wave velocity in sediments with higher-mode Rayleigh waves, *Geophys. Prospect.,* **35,** 187–196.

Giese, P., 1957. Die Bestimmung der elastischen Eigenschaften und der Mächtigkeit von Lockerböden mit Hilfe von speziellen Rayleigh-Wellen, *Gerl. Beitr. z. Geophys.,* **66,** 274–312.

Gucunski, N. & Woods, R.D., 1991. Inversion of Rayleigh wave dispersion curve for SASW test, in *Soil Dynamics and Earthquake Engineering V,* pp. 127–138, Institut für Bodenmechanik und Felsmechanik der Universität Karlsruhe, Elsevier, London.

Howell, B.F., Jr, 1949. Ground vibrations near explosions, *Bull. seism. Soc. Am.,* **39,** 285–310.

Jones, R., 1958. *In-situ* measurement of the dynamic properties of soil by vibration methods, *Geotechnique,* **8,** 1–21.

Jones, R., 1962. Surface wave technique for measuring the elastic properties and thickness of roads: theoretical development, *Brit. J. Appl. Phys.,* **13,** 21–29.

Kennett, B.L.N., 1983. *Seismic Wave Propagation in Stratified Media,* Cambridge University Press, Cambridge.

Klein, G., Bohlen, T., Theilen, F. & Milkereit, B., 2000. OBH/OBS versus OBC registration for measuring dispersive marine Scholte waves, in *62nd Conf. and Technical Exhibition, Expanded Abstracts,* EAGE, Glasgow.

Kodera, K., de Villedary, C. & Gendrin, R., 1976. A new method for the numerical analysis of non-stationary signals, *Phys. Earth planet. Inter.,* **12,** 142–150.

Köhler, R., 1935. Dispersion und Resonanzerscheinungen im Baugrund, *Zeitschr. techn. Phys.,* **12,** 597–600.

Köhler, R. & Ramspeck, A., 1936. Die Anwendung dynamischer Baugrunduntersuchungen, Veröffentlichungen des Instituts der Deutschen Forschungsgesellschaft für Bodenmechanik (Degebo) an der Technischen Hochschule Berlin.

Korschunow, A., 1955. On surface-waves in loose materials of the soil, *Geophys. Prospect.,* **3,** 359–380.

Kovach, R.L., 1978. Seismic surface waves and crustal and upper mantle structure, *Rev. Geophys. Space Phys.,* **16,** 1–13.

McMechan, G.A. & Yedlin, M.J., 1981. Analysis of dispersive waves by wave field transformation, *Geophysics,* **46,** 869–874.

Misiek, R., 1996. Surface waves: application to lithostructural interpretation of near-surface layers in the meter and decameter range, *Dissertation,* Institut für Geophysik, Ruhr-Universität Bochum, Germany.

Morse, P.M. & Feshbach, H., 1953. *Methods of Theoretical Physics,* Vol. 1, McGraw-Hill, New York.

Müller, G., 1985. The reflectivity method: a tutorial, *J. Geophys.,* **58,** 153–174.

Nazarian, S., 1984. *In situ* determination of elastic moduli of soil deposits and pavement systems by spectral-analysis-of-surface-waves method, *PhD thesis*, The University of Texas, Austin.

Nolet, G. & Dorman, L.M., 1996. Waveform analysis of Scholte modes in ocean sediment layers, *Geophys. J. Int.,* **125,** 385–396.

Okal, E., 1978. A physical classification of the Earth's spheroidal modes, *J. Phys. Earth,* **26,** 75–103.

Park, C.B., Miller, R.D. & Xia, J., 1999. Higher mode observation by the MASW method, in *Expanded Abstracts,* Society of Exploration Geophysicists.

Press, F. & Dobrin, M.B., 1956. Seismic wave studies over a high-speed surface layer, *Geophysics,* **21,** 285–298.

Roth, M., Holliger, K. & Green, A., 1998. Guided waves in near-surface seismic surveys, *Geophys. Res. Lett.,* **25,** 1071–1074.

Schalkwijk, K.M., 1996. Use of scattered surface waves to detect shallow buried objects, *Final report,* Institute of Earth Sciences, Utrecht University.

Schneider, C. & Dresen, L., 1994. Oberflächenwellendaten zur Lokalisierung von Altlasten: Ein Feldfall, *Geophys. Trans.,* **39,** 233–253.

Sezawa, K. & Kanai, K., 1935. Discontinuity in the dispersion curves of Rayleigh waves, *Bull. Earthq. Res. Inst.,* **13,** 237–244.

Sommerfeld, A., 1978. *Partielle Differentialgleichungen der Physik, Vorlesungen über Theoretische Physik,* Vol. 6, Harri Deutsch, Thun, Frankfurt.

Stokoe, K.H., II & Nazarian, S., 1983. Effectiveness of ground improvement from spectral analysis of surface waves, in *Proc. 8th Eur. Conf. on Soil Mechanics and Foundation Engineering,* Helsinki.

Tokimatsu, K., Tamura, S. & Kojima, H., 1992. Effects of multiple modes on Rayleigh wave dispersion characteristics, *J. Geotech. Engng.,* **118,** 1529–1543.

von Hartmann, H., 1997. Die Anwendung von Love-Wellen für die Untersuchung lateral inhomogener Medien bei ingenieurgeophysikalischen Aufgabenstellungen, *Dissertation,* Technische Universität Clausthal.

Wielandt, E. & Schenk, H., 1983. On systematic errors in phase-velocity analysis, *J. Geophys.,* **52,** 1–6.

Woodhouse, J., 1988. The calculation of eigenfrequencies and eigenfunctions of the free oscillations of the Earth and the Sun, in *Seismological*

Algorithms, pp. 321–370, ed. Doornbos, D.J., ch. IV.2, Academic, London.

Xia, J., Miller, R.D. & Park, C.B., 1999. Estimation of near-surface shear-wave velocity by inversion of Rayleigh waves, *Geophysics,* **64,** 691–700.

Xia, J., Miller, R.D. & Park, C.B., 2000. Advantages of calculating shear-wave velocity from surface waves with higher modes, in *Expanded Abstracts,* Society of Exploration Geophysicists.

APPENDIX A: PHASE-SLOWNESS ANALYSIS

Phase velocities may be derived from the phase $\varphi(\omega, r)$ of the Fourier coefficients

$$\tilde{u}(\omega, r) = A(\omega, r)\exp[i\varphi(\omega, r)] \tag{A1}$$

if the corresponding waveforms are single-mode plane waves (then $A(\omega, r)$ will vary only slowly with r). If they are not, the outcome of phase-difference techniques is unpredictable.

The phase

$$\varphi(\omega, r) = p(\omega)\omega r \tag{A2}$$

of a single plane mode is a linear function of the offset. The derivation of its absolute value from the Fourier coefficients is ambiguous by an additive constant of an integer multiple of 2π. This is due to the non-uniqueness of the involved arctan- or complex ln-function. However, for a wide frequency range the phase increment from r_l to r_{l+1} is certainly less than 2π. For this reason we use the advantage of a dense geophone spread and derive the phase traveltime

$$T(\omega, r_l) = \sum_{k=2}^{l} \frac{-i}{\omega} \ln[\tilde{u}(\omega, r_k)/\tilde{u}(\omega, r_{k-1})] \tag{A3}$$

relative to offset r_1. Then we fit a straight line

$$T_{\text{fit}}(\omega, r) = p(\omega)r + c \tag{A4}$$

to the $T(\omega, r_l)$ values at each frequency. Some offsets at both ends of the spread may be discarded if this improves the fit. The gradient $p(\omega)$ is the sought phase slowness at angular frequency ω.

APPENDIX B: GROUP-SLOWNESS ANALYSIS

The spectrogram (Gabor matrix) as shown in Fig. 10 is defined by

$$f(\omega, t) = \int_{-\infty}^{+\infty} u(t', r)h(t' - t)\mathrm{e}^{i\omega t'}\,dt' \tag{B1}$$

with a Gaussian taper

$$h(\tau) = \exp[-(\tau/\sigma)^2]. \tag{B2}$$

This essentially is the Fourier transform of a tapered version of the waveform with the taper centred at t. $\sigma = 53$ ms was used for Fig. 10, which means a half-width of 90 ms for the taper.

Properties of this 'moving-window analysis' are discussed by Kodera *et al.* (1976) and Wielandt & Schenk (1983).